Journal of Colloid and Interface Science 540 (2019) 544–553

Contents lists available at ScienceDirect

Journal of Colloid and Interface Science

journal homepage: www.elsevier.com/locate/jcis

Contact line stick-slip motion and meniscus evolution on micrometer-size wavy fibres

C.A. Fuentes [a,*], M. Hatipogullari [b], S. Van Hoof [a], Y. Vitry [b], S. Dehaeck [b], V. Du Bois [a], P. Lambert [b], P. Colinet [b], D. Seveno [a], A.W. Van Vuure [a]

[a] Department of Materials Engineering, KU Leuven, Leuven, Belgium
[b] TIPs (Transfers, Interfaces, and Processes), Université Libre de Bruxelles, Bruxelles, Belgium

GRAPHICAL ABSTRACT

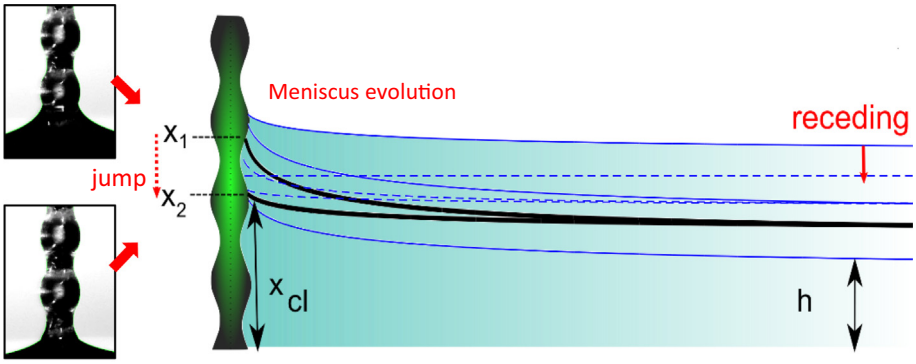

ARTICLE INFO

Article history:
Received 24 October 2018
Revised 10 January 2019
Accepted 11 January 2019
Available online 14 January 2019

Keywords:
Wetting
Stick-slip contact line motion
Wavy fibers
3D printing
Meniscus shape
Goniometer
Tensiometer

ABSTRACT

Hypothesis: The architecture of complex-shaped fibres affects the motion of the contact line and the evolution of its associated menisci when a fibre is immersed into a liquid. Understanding and predicting the motion of the contact line is critical in the design of complex-shaped fibres for many engineering applications as well as for surface science. While wetting on classic circular cylinders has been well studied, singularities during the wetting process of complex-shaped fibres are not yet well understood.
Experiments: The dynamic wetting behaviour of axisymmetric sinus-shaped fibres immersed vertically in a liquid volume was investigated. Fibres were 3D-printed down to micrometre dimensions, and the Wilhelmy method was used in parallel with meniscus shape analysis. Moreover, a quasi-static theoretical model predicting the contact line movement and free energy of the system evolution on these fibres is also proposed.
Findings: The observation of liquid advancing and receding fronts highlighted a stick-slip motion of the meniscus depending on both the fibre surface curvature and its intrinsic wettability. The model predicts that the behaviour of the seemingly pinned and then jumping contact line, with associated changes in apparent contact angles, can be explained by the interplay between a constant local contact angle and the movement of the bulk liquid, leading to the storage of energy which is suddenly released when the contact line passes a given point of fibre curvature. Besides, acceleration/deceleration events that take place before and after the jumps are experimentally observed in good agreement with the model.

* Corresponding author.
E-mail address: Carlos.Fuentes@kuleuven.be (C.A. Fuentes).

https://doi.org/10.1016/j.jcis.2019.01.045
0021-9797/

1. Introduction

Wetting forces and analysis of meniscus shape formed around fibres immersed perpendicularly into a liquid have been traditionally used to study the wettability of single fibres, which is essential in several technological applications, such as fibre reinforced composite design [1–3] and coating of textile fibres [4]. The measurement of the capillary force exerted by a liquid on a fibre, from which a contact angle can be calculated, is known as the Wilhelmy method (tensiometry) [5]. This pull or push force is produced by the weight of displaced liquid above or below the reference horizontal free surface [6]. An advancing meniscus is formed when the fibre is immersed into a liquid, while a receding meniscus is observed when the fibre is withdrawn from the liquid. In general, both situations correspond to different apparent contact angles and not to a single value, as theoretically predicted by Young's equation for an ideal surface. This so-called hysteresis is related to the pinning of the contact line at physical or/and chemical heterogeneities [7,8]. Moreover, the value of the experimentally measured contact angle is also influenced by the velocity of the advancing and receding fronts [3,9,10]. The Wilhelmy technique has high accuracy when measuring contact angles of fibres with regular shape [3,11]. However, the analysis of the wetting behaviour of irregular fibres (i.e. wavy and rough natural fibres) using this technique is reported to be very challenging since small variations in the fibre perimeter can largely affect the capillary force and hence the calculated contact angles [12,13].

Alternatively, the wetting behaviour of a single fibre can also be studied by goniometry, i.e. observing the shape of a steady meniscus formed when a vertical fibre is brought in contact with a liquid. This technique relies on the localization and modelling of the liquid/vapour interface when the fibre is partially immersed in a liquid volume. A simple modelling procedure could involve a proper fit of the meniscus profile by a polynomial or spline functions [14]. However, the contact angles obtained are then generally not accurate since the results are often highly influenced by the choice of a given mathematical function with no physical basis that cannot fit the drastic change in the interface curvature for a wide range of contact angles [2,15,16]. For instance, Bateni et al. [17] showed that contact angles calculated using the slope of a polynomial at the contact point vary according to the degree of the polynomial and the number of pixels used in the fitting procedure.

A more accurate approach is to use a mathematical model with a sound physical description of the shape of the meniscus [2,18,19]. In static and quasi-static conditions, the liquid/vapour interface is well described by the Young-Laplace equation [20–22]. If the gravitational effects are neglected (typically when the Bond number $Bo = \frac{\rho g r^2}{\Upsilon} \ll 1$, with ρ the liquid density, g the gravity acceleration, r the fibre radius, and Υ the liquid-air surface tension), an analytical solution to the Young-Laplace equation for a liquid wetting a cylindrical fibre can be used to describe the corresponding meniscus shape [20,21]. Then, the contact angle can be simply extracted by measuring the meniscus height and fibre radius [21,23]. For systems where gravity cannot be neglected, the Young-Laplace (non-linear second-order differential) equation has generally to be numerically solved by using, for instance, a first order Runge-Kutta algorithm [19]. The (quasi) static regime holds as long as the capillary number $Ca = \frac{\eta V}{\Upsilon}$ (with η the liquid dynamic viscosity, and V the contact line velocity) is small; otherwise, dynamical models should be used [24].

Almost all the models previously described for measuring the wettability of fibres have been developed for the characterization of the menisci on perfect circular cylinders, while fibres with more complex shapes have received less attention [25–27]. Irregular natural fibres [12] and the recent development of complex-shaped fibres for industrial applications, such as hollow glass [28] and expanded/ablated fibres [29,30] for improving composite interfaces, call for new studies focusing on the particular features (e.g. diameter change along the fibre length) encountered during the motion of the contact line on fibres with non-circular and variable cross sections [25,31,32]. An analysis of the meniscus shape on such complex-shaped fibres needs the development of new experimental techniques and the validation or improvement of traditional theoretical models.

In this study, the dynamic wetting behaviour of an axisymmetric sinus-shaped fibre (wavy fibre) immersed vertically in a large liquid volume has been investigated. Fibres were computer-designed and 3D printed down to micrometre dimensions with Nanoscribe Photonics GT equipment, and the Wilhelmy method was used in parallel with meniscus shape analysis; these two independent techniques were being cross-validated by direct comparison of resulting contact angles. This methodology enabled monitoring the profile of the fibre and the liquid meniscus while the fibre was being immersed, and to correlate the contact angle variations with the motion of the contact line.

The immersion and withdrawal of the fibre resulted in stick-slip motion of the meniscus [27,33–36], which is predicted by a quasi-static model directly inspired by an analysis of the impact of chemical heterogeneities on stick-slip behaviour and hysteresis in a microchannel [37]. Static model solutions are here tracked upon varying the immersion depth in upward and downward directions, explaining why two different paths for the contact line position are observed, with pinning-depinning events occurring in both cases.

2. Methodology

2.1. Materials

Sinus-shaped fibres were 3D printed with a Photonic Professional GT laser lithography system (Nanoscribe GmbH, Germany) by direct laser writing of an acrylic based negative tone resist (IP-G 780), with a 3D resolution of 600 nm. All fibres were printed following a sinusoidal wave with a diameter of 150 μm at peak amplitude and a period of 200 μm, while the diameter at the lowest amplitude was designed with 4 different values: 80, 100 (Fig. 1a), 120, and 140 μm. These fibres will be further referred to as 150/80, 150/100, 150/120, and 150/140 respectively. All fibres also contain a perfect circular cylinder portion with a diameter of 150 μm and a length of 5 mm at both fibre ends. The quality of the printed fibres is examined in supporting material SM1.

2.2. Tensiometric method

Advancing and receding contact angles of ultrapure water (18.2 Ω cm resistivity, γ = 72.8 mN/m) were measured on the fibres at room temperature (20 °C) and relative humidity of 65%, using a Krüss K100 SF tensiometer equipped for the Wilhelmy technique with a resolution of 0.1 μg. This technique consists in measuring the forces exerted by a liquid on a solid substrate with known perimeter while the substrate is vertically and partially immersed into the test liquid and then withdrawn [12]. The fibre is actually not displaced, but the vessel containing the liquid moves up (h defined in Fig. 1b increases) and down (h decreases) during an advancing-receding cycle.

When the fibre is immersed into the liquid, the microbalance measures a force ($F_{measured}$), which is the sum of the capillary force ($F_{wetting}$), the weight of the fibre (W) and the buoyancy force ($F_{buoyancy}$):

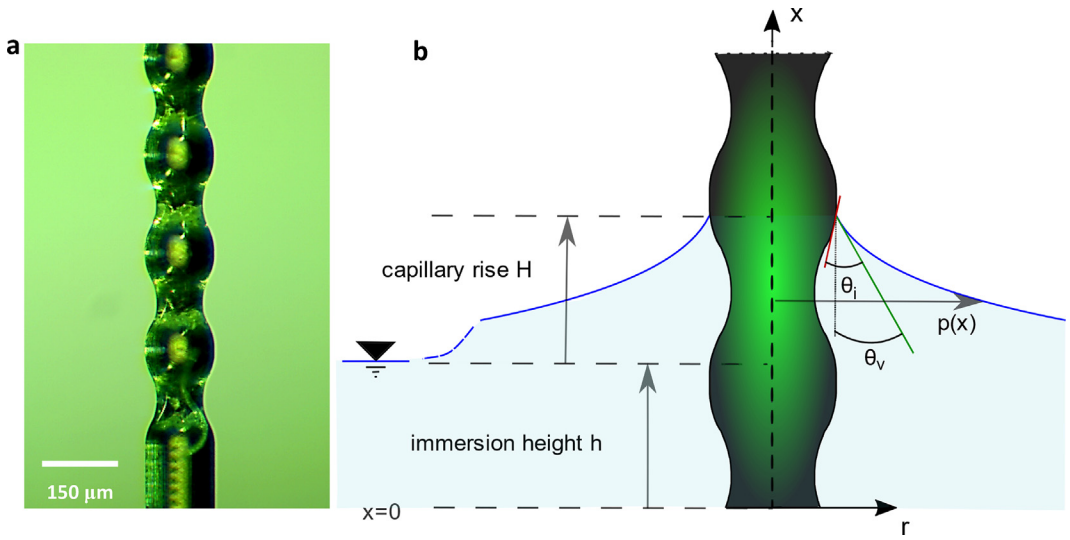

Fig. 1. (a) Optical microscopy of a 150/100 fibre. (b) Definition of terms: x is the axial coordinate attached to the fibre; the level of the liquid bath is at $x = h$; the contact line is at $x_{CL} = h + H$ (with H the capillary rise) where the meniscus makes an angle θ_i with the fiber, and θ_V with the vertical.

$$F_{measured} = F_{wetting} + W - F_{buoyancy} = 2\pi r\gamma \cos\theta_V + mg - \pi\rho g \int_0^{x_{cl}} r^2(x)dx \quad (1)$$

where r is the fibre radius, m the fibre mass, and x_{CL} the contact line position. When the weight of the probe is measured beforehand and set to zero on the balance, only the wetting and buoyancy forces remain:

$$F_{measured} = 2\pi r\gamma \cos\theta_V - \pi\rho g \int_0^{x_{cl}} r^2(x)dx \quad (2)$$

The buoyancy term is a factor $\frac{\pi x_{CL}}{l_c^2}$ smaller than the wetting term, with l_c the capillary length of water (2.7 mm) and hence accounts maximally a few percent of the measured force. All dynamic contact angle measurements were conducted at a velocity of 0.5 mm/min and with a 0.01 mm data sampling step. By synchronizing the tensiometric method with the goniometric technique (Section 2.3), it was possible to extract apparent contact angle θ_V data from the tensiometer trace. The synchronization is explained in supporting material SM2.

Advancing and receding angles are considered in this paper as the highest and lowest metastable contact angle respectively, that can be measured by the method described before.

2.3. Goniometric method

Samples were imaged using a Motic SMZ-171-TH microscope and a 3664x2748 pixel Moticam camera (Motic Deutschland GmbH, Wetzlar, DE) using a one second picture interval with an exposure of 700 ms. The resolution of the images was 0.213 µm/pixel. Image acquisition was recorded and synchronized with the tensiometer, ensuring that the weight of the meniscus is recorded at the same time as the image of the meniscus is acquired.

Due to the low velocity (V), 0.5 mm/min, used in all experiments and the physical parameters of water (η = 1.0 mPa.s), the capillary number (Ca) for water remains very small: $1.14x10^{-7}$. Under these conditions, the liquid/vapour interface has a quasi-static profile satisfying the Young-Laplace equation. The contour shape of the meniscus was fitted by this theoretical profile thanks to a modified version of the G-fibre in-house software [19]. Details of this method can be consulted in [15,19].

The G-fibre software was modified to calculate apparent contact angles (θ_v in Fig. 1) on sinus-shaped fibres by assuming a perfect circular cylinder of a given radius at a specific location of the contact line (x_{cl}). Then, the angle θ_i between the profile and the fibre can be computed using Eq. (3) since the geometry of the fibre is known.

$$\theta_V(x_{cl}) = \theta_i(x_{cl}) - \text{atan}(r'(x_{cl})) \quad (3)$$

3. Results and discussion

3.1. Wetting behaviour of an axisymmetric sinus-shaped fibre

Fig. 2a–e shows a 150/100 fibre being immersed in water (see movie clip MC1 in Supporting Material). When the fibre is put into contact with the liquid, the liquid surface deforms spontaneously and rises up on the fibre to form a meniscus, with a three-phase contact line located above the horizontal liquid surface of the reservoir (Fig. 2a). When the vessel containing the liquid moves up, the liquid surface induces a vertical displacement of the contact line; but the contact line does not move to the same extent as the bulk liquid (see Supporting Material 2), where the contact line is eventually located below the horizontal liquid surface due to an apparent contact angle higher than 90° (see shadow due to contact line surrounded by water in Fig. 2b–d). Finally the contact line moves very fast to a higher position, i.e. it undergoes a jump (Fig. 2e).

A similar behaviour occurred during the receding process, as can be seen in Fig. 2f–j and movie clip MC2 (attached as Supporting Material), although in this case the horizontal liquid surface is moving downwards. At a given moment also the contact line movement slows down (see Supporting Material 2) in comparison to the position of the horizontal liquid surface, and finally the contact line suddenly jumps to a lower position (Fig. 2j).

These sudden jumps in the contact line position x_{CL} can be explained by the statics of capillary rise on a sinusoidal fibre starting from a liquid reservoir level h, the experimentally controlled parameter, which is increased or decreased when immersing or withdrawing the fibre respectively. Fig. 3 shows a schematic representation of the receding process (the explanation of the advancing process is analogous).

In Fig. 3a, static menisci are drawn on various contact line positions x_{CL}, satisfying the Young-Laplace Ordinary Differential Equation (ODE),

$$x'' = (1+x'^2)\left[\frac{1}{l_c^2}x\sqrt{1+x'^2} - \frac{x'}{p}\right] \quad (4)$$

in which primes denote derivation with respect to p (all symbols are explained in Fig. 1b), all lengths are scaled with the radius $r(x_{cl})$, and l_c is the capillary length of water. This ODE is closed by imposing (i) $x'(1) = -\cot\theta_V = -\cot(\theta_i - a\tan(r'(x_{cl})))$ at the fibre at an angle relative to the vertical, and (ii) $x'(+) = 0$, that is to say, the meniscus becomes flat far away from the fibre (θ_i is taken here as the experimentally measured receding angle, see Table 1). Convergence is achieved by taking a domain size of $50l_c$. The calculation of these profiles involves the radius $r(x_{CL})$ and apparent angle $\theta_V(x_{CL})$ evaluated on the contact line position. The case where the fibre displays intrinsic contact angle hysteresis is treated later in Section 3.4.

If we start an experiment with the uppermost drawn configuration of the liquid/air interface, decreasing the liquid bath level h results in the contact line descending on the fibre. This situation continues until the configuration of the liquid/air interface corresponds to $h = h^*$ and $x_{cl} = x_1$ (drawn in black in Fig. 3a). From this configuration on, displacing the contact line downwards would require increasing h. The configurations of the liquid/air interface, with $x_{cl} < x_1$ but $h > h^*$, are drawn in dashed lines in Fig. 3a. Although they start at a lower position on the fibre, their apparent angles θ_V are high enough (due to the local waviness of the fibre) such that these interfaces already become flat at an immersion height $h > h^*$, which is violating the experimental constraint that$h$ must decrease. The contact line then jumps from a position x_1 to x_2 at a constant immersion depth $h = h^*$.

Note that in order to predict the jumps, it suffices to calculate the equilibrium rise height H on each point of the fibre (see Fig. 1). As the studied fibres are much thinner than the capillary length of water l_c, the equilibrium height H of the capillary rise/depression can be calculated by adapting the formula existing for a straight fibre [21] to the case of an heterogeneous fibre considered here. For each given contact line position x_{cl}, one then readily obtains

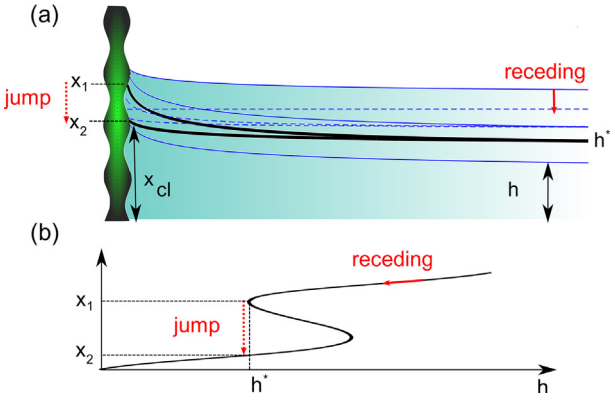

Fig. 3. Explanation of the jump observed when a sinus-shaped fibre is withdrawn. (a) For different contact line positions, static menisci with the same contact angle θ_i measured locally on the fibre are drawn. When the meniscus is receding (decreasing h), at the immersion height $h = h^*$, a jump of the contact line position occurs from x_1 to x_2, skipping the menisci drawn in dashed lines as they correspond to $h > h^*$. (b) Corresponding graph of the contact line positionx_{cl} versus the experimentally controlled immersion height h. Following the graph from right to left requires the contact line to jump.

Table 1
Measured advancing and receding angles on the cylindrical portions of the 3D printed fibres and corrected (using Eq. (3)) contact angles on the wavy portions.

Diameter at lowest amplitude (μm)	Advancing CA $\theta_V = \theta_i = \theta_A$[°] on cylindrical portion tensiometer	Receding CA $\theta_V = \theta_i = \theta_R$[°] on cylindrical portion tensiometer	Local receding CA $\theta_i = \theta_R$[°] on wavy portion goniometer
80	76.6 ± 0.6	45.4 ± 0.9	45.1 ± 1.4
100	76.1 ± 0.8	45.3 ± 1.0	45.0 ± 1.4
120	77.4 ± 1.0	42.8 ± 1.1	43.3 ± 1.7
140	77.8 ± 1.1	45.4 ± 1.0	43.9 ± 1.1

$$H(x_{cl}) \cong r(x_{cl})\cos\theta_V(x_{cl})\left[\ln\left(\frac{4l_c}{r(x_{cl})(1+\sin\theta_V(x_{cl}))}\right) - C\right] \quad (5)$$

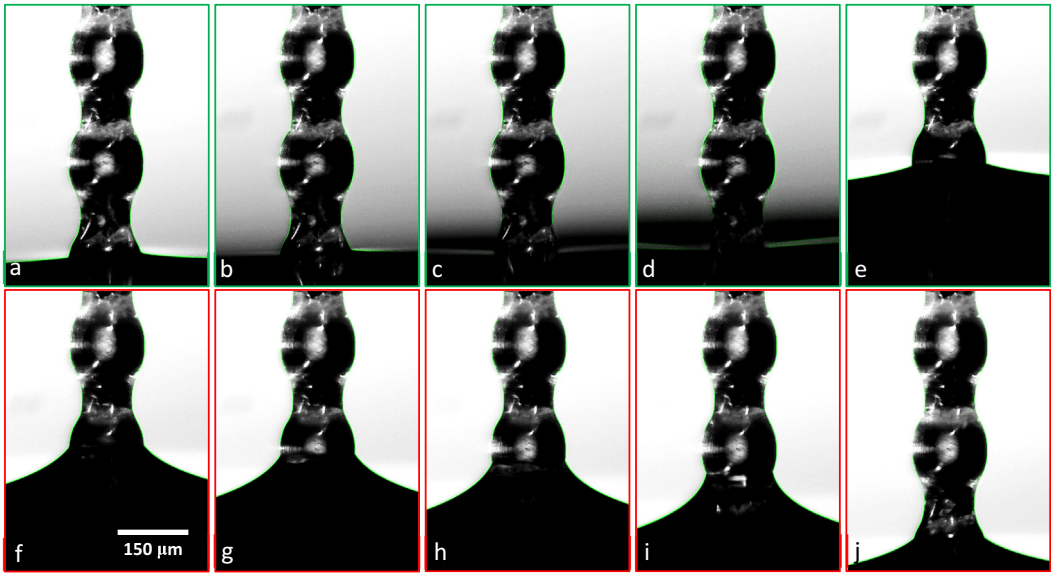

Fig. 2. Meniscus shape during immersion into water for an advancing (a–e, green border) and for a receding (f–j, red border) contact line of a sinus-shaped 150/100 fibre. Images taken at equal time intervals (2 s). (For interpretation of the references to colour in this figure legend, the reader is referred to the web version of this article.)

where C is the Euler constant (0.57721...), and $r(x)$ is the local radius, as described in Fig. 1. From this point forward, unless stated otherwise, the term *model prediction* will be use to refer to the results obtained using Eq. (5).

In the studied range of r and θ_V, Eq. (5) is found to approach the solution of the Young-Laplace ordinary differential equation ODE (Eq. (3)), with an error below 0.17%. Fig. 3b shows the position of the horizontal liquid surface h, calculated for every possible contact line position x_{cl} as

$$h(x_{cl}) = x_{cl} - H(x_{cl}) \tag{6}$$

Notably, not only one but three equilibrium contact line positions x_{CL}exist for a range of liquid bath levels h, out of which the middle one is unstable (as shown later in Section 3.2). In this range of h, the observed x_{CL}, and thereby the quantities which depend on it, such as the apparent angle θ_V, display hysteresis induced by the waviness of the fibre. Namely their value depends on whether Fig. 3b is followed from right to left (receding), or from left to right (advancing). In both directions a jump occurs where $\frac{dh}{dx_{CL}} = 0$.

This model explains the observed jumps and hysteresis upon experimentally varying the liquid bath level h in a qualitatively similar way as the explanation of the jumps and hysteresis for a moving liquid wedge over a chemical defect upon varying the contact line position far from the defect [27], a drop on a chemically heterogeneous substrate upon varying its volume [34], and a liquid in a chemically heterogeneous microchannel upon varying its volume [32].

3.2. Energy dissipation during the jump

The effect of the jump on the free energy of the system is evaluated by the analysis of the force trace during wetting of the fibre (Eq. (2)), as can be seen in Fig. 4a. The calculated force trace shows that the work gained by dipping the fibre over one wavelength (area under the green curve) is smaller than the work required to withdraw the fibre over one wavelength (area under the red curve). More specifically, an advancing-receding cycle over one wavelength dissipates 1.76 nJ of energy.

In order to evaluate how this dissipated energy was integrated in the system, the free energy of the system G is calculated, which is given by the integration of the interfacial tensions along the surfaces on which they act as well as by the gravitational potential energy of the meniscus (indexes $_{sa}$, $_{sl}$ and $_{la}$ stand for solid-air, solid-liquid, and liquid-air respectively).

$$G = \gamma A_{la} + \int \gamma_{sa} dA_{sa} + \int \gamma_{sl} dA_{sl} + \rho g \int x dV \tag{7}$$

Introducing the intrinsic contact angle θ_i by Young's law, the free energy (up to a constant) is given by

$$\Delta G = \gamma A_{la} - \gamma cos\theta_i A_{sl} + \rho g \pi \int_h^{x_{cl}} (x-h)(p^2 - r(x)^2) dx \tag{8}$$

where the interface areas between liquid-air (A_{la}) and solid-liquid (A_{sl}) are calculated as revolution integrals, and the profile $p(x)$ of the meniscus, as a function of the axial coordinate (as defined in Fig. 1b), is obtained by solving the Young-Laplace equation (Eq. (4)). Under the constraint of an imposed immersion depth h, the first term makes the system to favour configurations in which the liquid-air interface is minimal, i.e. $\theta_V \to 90°$, while the second term describes the energy gain by wetting the fibre area, because the fibre is wettable ($\cos\theta_i > 0$). The third term describes the energy cost of elevating the meniscus mass above the reservoir level.

Fig. 4b shows a clearer picture on the dissipated energy over one wavelength using Eq. (8). Starting from $h = 100$ μm, one random position in the single-valued range of h where the free energy value corresponds to 9.30 nJ, dipping the fibre (increasing h) results in a continuous reduction of the free energy of the system as the fibre is wettable. When $h = 300$ μm is reached (i.e. after 200 μm, one wave length), after the in-between advancing jump at $h = 243$ μm, the free energy of the system corresponds to 5.38 nJ. Then, the free energy of the system was reduced by 3.92 nJ, of which 1.09 nJ is dissipated during the advancing jump. To go back to $h = 100$ μm, the system requires 4.59 nJ, of which 0.67 nJ will be dissipated during the receding jump at $h = 138$ μm, making a total dissipated energy of 1.76 nJ in an advancing-receding cycle over one wavelength.

Fig. 3a also shows a schematic representation of withdrawing the fibre from water with the position of the horizontal liquid surface h as the experimentally controlled parameter, while the contact line position x_{cl} results from the physics of the capillary rise. The liquid-air interface area continuously increases while θ_V decreases during the receding process, until the receding contact line reaches position x_1, where the jump occurs. Thus, in this range

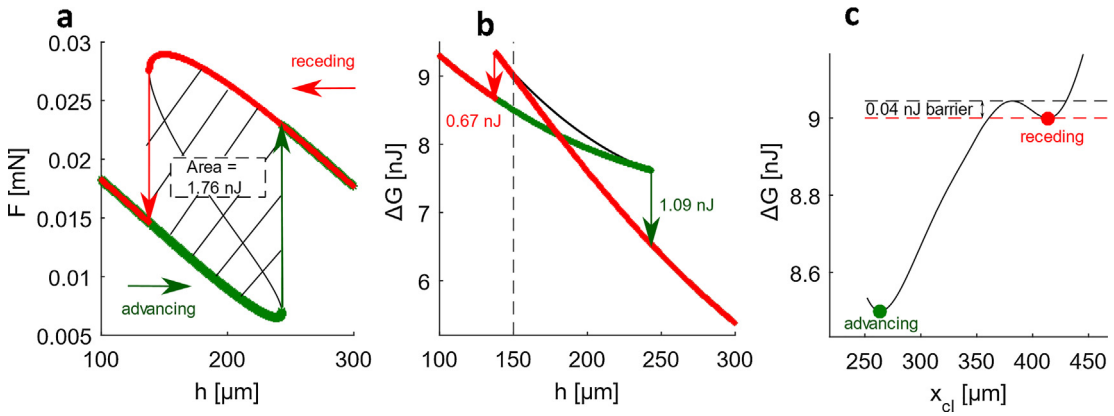

Fig. 4. Energy dissipated in the jumps; (a): force exerted on the fibre (Eq. (2)) versus immersion depth h. black: all static solutions, green: subset of stable static solutions, tracked upon increasing h (advancing), red: stable solutions tracked upon decreasing h (receding). (b): with the same colour code, free energy of equilibrium configurations (contact angle θ_i is equal to its equilibrium value) as a function of h, the vertical dotted line corresponds to an arbitrary constant immersion height of 150 μm. (c) free energy as a function of x_{CL} at$h$ equal to 150 μm, where the contact angle θ_i is now a free parameter. The red and green dot correspond to the equilibrium configurations encountered in the receding and advancing path respectively. (For interpretation of the references to colour in this figure legend, the reader is referred to the web version of this article.)

of h values, the system stores the energy that is provided to decrease h in its liquid-air interface and as gravitational potential energy. Immediately after the jump, the contact line is at x_2 with a lower liquid-air interface area and gravitational potential energy. This means that during the jump, which occurs at constant $h = h^*$, part of the stored energy is used to dewet the fibre from x_1 to x_2, while 0.67 nJ still needs to be dissipated as the system cannot keep storing it at the equilibrium state that the system attains after the jump.

Fig. 4b also shows that although multiple equilibrium configurations exist in a range of h values, still one of them has a lower free energy than the others. In this range, the free energy as a function of x_{CL} (drawn for an arbitrary height $h = 150$ µm in Fig. 4c) shows that both the advancing and receding solutions (presented as dots) are local minima of the free energy, with a local maximum in between which acts as an energy barrier to trap the system in a metastable configuration. This result, proven analytically in the configuration of a drop on a chemically heterogeneous substrate [33] and a liquid in a microchannel with chemically heterogeneous walls [37], is recovered here numerically for this configuration.

For the situation drawn in Fig. 4c, the system is trapped in the receding configuration (red dot). This local minimum is separated from the advancing configuration (green dot) by a local maximum. In order to move from one metastable to the other, the system would have to overcome the barrier of 0.04 nJ, and then the advancing jump will take place and dissipate 0.54 nJ, reaching the minimum energy configuration indicated with the green dot. This energy barrier can for example be overcome by vibrational noise [38,39]. But in absence of this situation, the system will proceed to recede along the red track in Fig. 4b, till the receding jump takes place at $h = 138$ µm.

3.3. Influence of the variation of the wave amplitude

In order to go deeper into the analysis of the influence of the fibre geometry on the wetting behaviour of wavy fibres, 4 different shapes were analysed, as explained in the methodology section. Fig. 5 shows the contact angle variation along the fibre length for the 4 different fibres using the analysis of the meniscus shape (goniometry) and the values obtained with the model during a receding process. Due to the fact that the horizontal liquid surface is above the contact line position during most of the advancing process, the meniscus shapes cannot be observed and henceforth only the receding process is analysed.

The surfaces of the fibres studied in the present paper are rough and/or chemically disordered at the nanoscale and can then normally be characterized by one advancing and one receding contact angle [7,40]. Advancing and receding angles were measured on the circular cylinder portion of the fibres and are reported in Table 1. In all cases, the advancing and receding angles are statistically the same, which makes sense since all fibres are made of the same material and the same fabrication procedure has been used (resulting in the same chemical composition and residual roughness). The measured contact angles remained unalterable after repeated cycles of immersion and withdrawal of the fibres, ensuring that the advancing and receding contact angles of water on the 3D printed fibres are stable and repeatable, and not affected by non-equilibrium phenomena (e.g. adsorption and diffusion) during the time scale of the experiments.

Furthermore, Fig. 5e–h shows the values of the contact angles θ_i with respect to the fibre (using Eq. (3)). The result is summarized in the last column of Table 1. For all geometries, θ_i values are statistically the same and also equal to the receding contact angle of the material. Therefore, in this section, we assume in our model

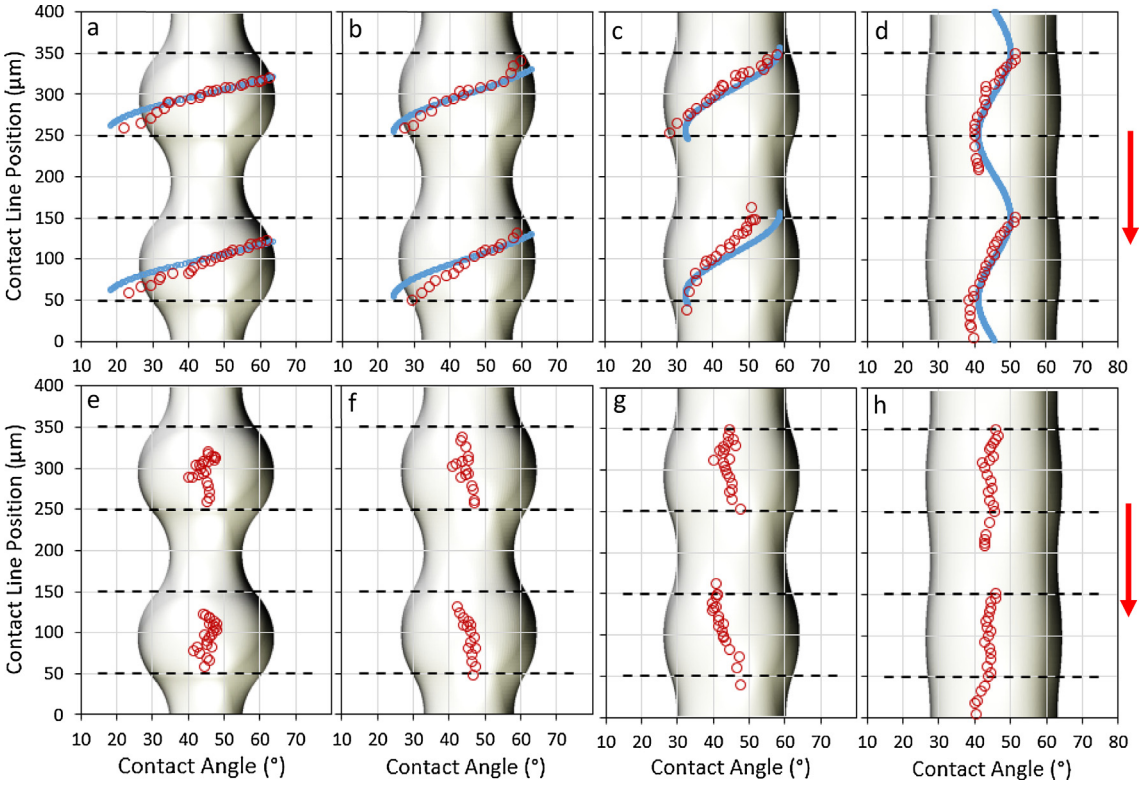

Fig. 5. Receding contact angles versus contact line position for the 4 types of 3D printed fibres: 150/80, 150/100, 150/120, and 150/140. Top: Apparent contact angle θ_v, data from the experiment (goniometer) in red and from the model (assuming capillary equilibrium with a receding angle θ_i of 45°) in light blue. Bottom: local contact angle θ_i. The dotted black lines show the positions of the inflexion points. Red arrow: direction of the contact line movement. (For interpretation of the references to colour in this figure legend, the reader is referred to the web version of this article.)

that the fibre is chemically homogeneous, with a wettability characterized by the measured receding angle. The only factor inducing the large variation of contact angle values θ_V along the wavy portion of the fibre is the geometry of the fibre surface.

All the configurations show the same behaviour. As the contact line goes down the fibre (receding front), the corresponding meniscus height is increasing, whilst the fluid is passing the concave sections on the fibres. Since the experimentally controlled parameter is the liquid surface level (which is the level from which the capillary rise starts), this leads to the observation that the contact line is 'slowing down', i.e. decreasing the liquid surface level by a certain distance leads to a decrease of the contact line position by a smaller distance. Despite the slow motion of the contact line, there is a considerable deformation of the liquid surface (see Fig. 2) since the meniscus is adapting to the shape of a given vertical apparent angle, which moves from 62° down to 22° for a 150/80 fibre (see Fig. 5). Finally, the contact line reaches a zone close to the inflection point (Fig. 5a, position 260 μm) and jumps to a lower position (Fig. 5a, position 123 μm).

The position of the contact line immediately before and after the jump is related to the geometry of the fibre and how large is the variation of the local perimeter. Fig. 5 reveals that there has been a slight fall of the jumping starting position from 259.7 μm to 258.8 μm, and to 253.2 μm for a 150/80, 150/100, and 150/120 fibre respectively. However, the 150/140 fibre showed a marked fall in the starting position of the jump, reaching a jumping position of 211.4 μm (see Fig. 5d). Of course, for a fully straight fibre, there would be no jump at all anymore. As it can be seen in Fig. 5a–c, the jumps of the contact line occur in a region close to the inflection point for the 150/80, 150/100, and 150/120 fibres.

The experimental displacement of the contact line after the jumps increases with the wave ratio (ratio of smallest to largest diameter of the fibre) as shown in Fig. 6a. The black dots correspond to 57.5 μm, 90.9 μm, 128.0 μm and 137.0 μm of displacement for the fibres with diameters of 140 μm, 120 μm, 100 μm, and 80 μm at the lowest amplitude respectively. The latter three fibres correlate well with the predictions of the model (full red line) which is based on tracking the static solutions while decreasing h (receding). We first proceed with the analysis of the wetting behaviour of these three fibres and come back to the situation of the 150/140 fibre later.

For the fibres 150/120, 150/100 and 150/80, the energy dissipated in the jumps is calculated from the tensiometer force trace (e.g. the trace of 150/80 is given later in Fig. 8) as the area $\int (F_R - F_A) dh$ between the receding and advancing force. First the area is measured between the traces corresponding to the wavy portion of the fibres, and divided by the wavelength, in order to obtain the average dissipated energy over a wavelength. Secondly, the dissipation due to the uncontrolled contact angle hysteresis is measured from the horizontal portion of the force trace, corresponding to the perfectly cylindrical portion of the fibre. The energy dissipated in one advancing and one receding jump can be then calculated by subtracting the dissipation due to the uncontrolled contact angle hysteresis (e.g. 3.03 nJ for 150/80 in Fig. 8). The experimental values of the dissipated energy increase with the wave ratio from 0.26 nJ to 1.00 nJ to 1.51 nJ for the 150/120, 150/100 and 150/80 fibres from left to right in Fig. 6b (black dots).

The procedure described above relies on the assumption that the total dissipated energy is equal to the dissipation due to contact angle hysteresis (nanoscale wetting heterogeneity) plus the energy dissipated during the jump events. The reasonable match between the experimental values and the model prediction (red line in Fig. 6), where the latter is calculated in the absence of a small-scale heterogeneity, verifies that this assumption can be taken here as a good approximation.

Both the experimental and numerical data suggest that the dissipated energy scales with jump distance to the fourth power (Fig. 6c). This scaling is especially accurate for low values of the jump length and dissipation, i.e. closer to the threshold of hysteretic behaviour [27,37,41]. The theoretical derivation of this scaling [37] consists of writing a Taylor series near the critical point (where $\frac{dh}{dx_{CL}} = \frac{d^2h}{dx_{CL}^2} = 0$) present at the threshold and is adapted in the supporting material SM3 for this specific case. It is different than the quadratic scaling that Shanahan [34] has predicted when the length scale of the pinning sites is much smaller than the system size (in that case the drop radius).

The threshold for a jump to take place is shown as a vertical dashed line in Fig. 6a and b, at a wave amplitude of 0.88 or a diameter of 132 μm at the lowest amplitude. Above this wave amplitude, only one equilibrium configuration exists at each fixed immersion depth h and $\frac{dh}{dx_{CL}} > 0$ for each x_{CL}. This is the case for fibres which are not 'wavy' enough, as in the case of the 150/140 fibre. For this situation the model predicts that the meniscus can contact the whole fibre in a continuous way without the necessity of jumping.

However, this appears to be inconsistent with the experimental observation of a jump (see Figs. 5d and 6a). Nevertheless, the model is still predicting a periodic variation of the contact line position with h. Experimentally, h is increased/decreased at con-

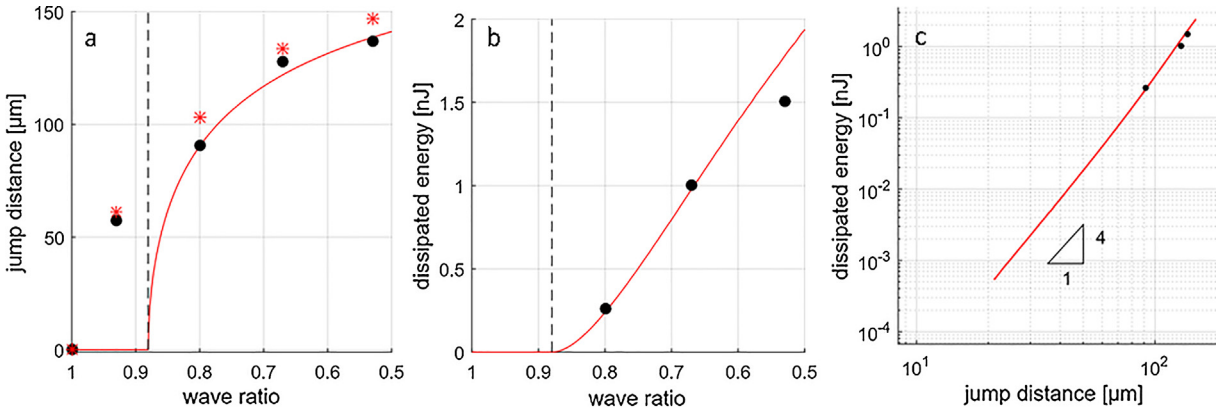

Fig. 6. (a) Jump distance as a function of the wave ratio (ratio between the lowest and largest radius) from experiment (black dots), model (red line) and corrected model data (red stars, assuming jumps when $\frac{\dot{x}}{\dot{h}} > 1.5$, with $\dot{x}$ and $\dot{h}$ is the contact line and horizontal liquid surface velocities respectively). The vertical dashed line represents the location of the threshold wave ratio (0.88) (b) Energy dissipated over one wavelength as a function of wave ratio. (c) Energy dissipated as a function of jump length. (For interpretation of the references to colour in this figure legend, the reader is referred to the web version of this article.)

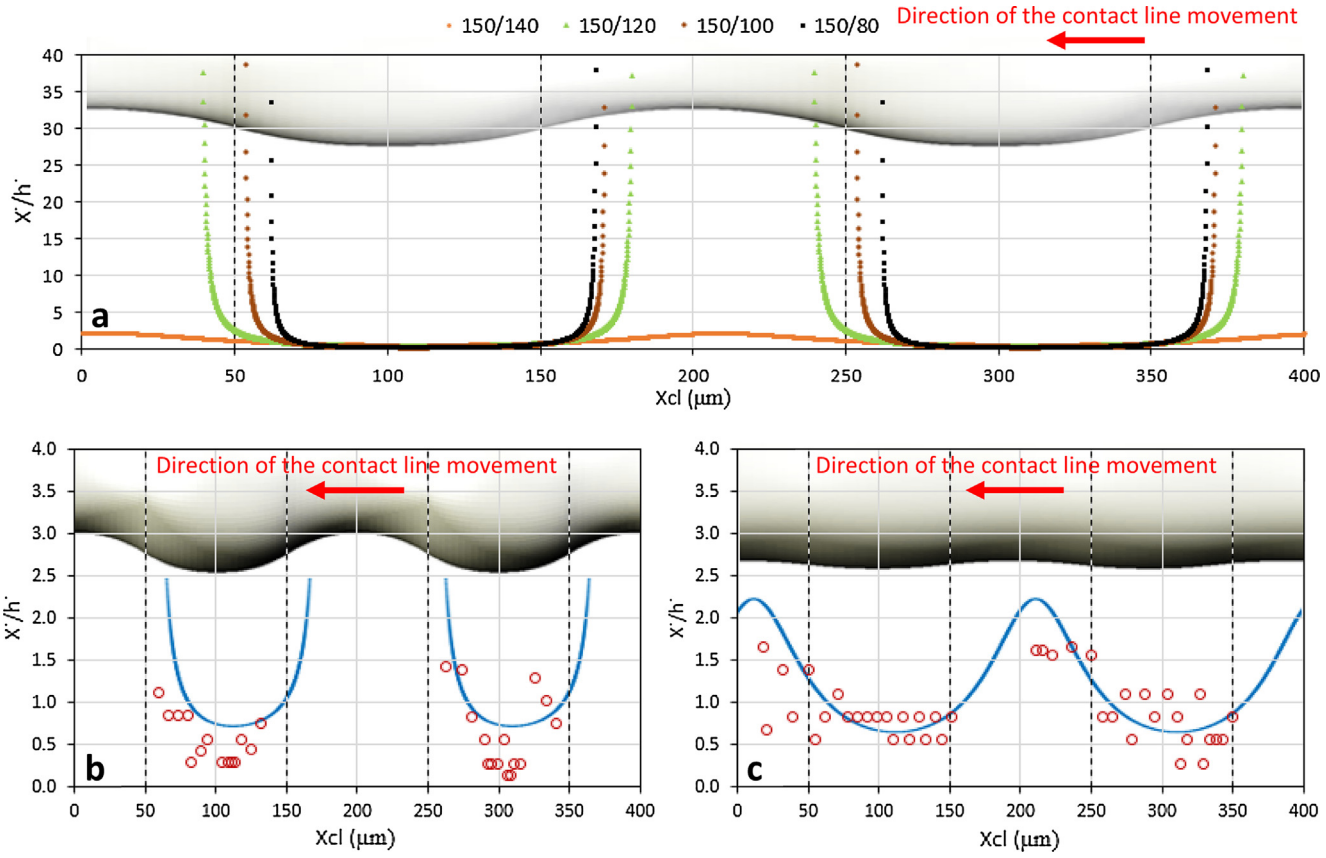

Fig. 7. Ratio of the contact line velocity to the withdrawal speed ($\dot{x}/\dot{h}$) as a function of the contact line position (x_{cl}) for the 4 different types of fibres (a), and comparison between the experimentally measured velocities (red circles) and model predictions (blue lines) for the 150/100 (b) and 150/140 (c) fibres respectively. (For interpretation of the references to colour in this figure legend, the reader is referred to the web version of this article.)

stant velocity, which means that the contact line needs to periodically accelerate and decelerate to stay close to equilibrium.

Fig. 7a shows the ratio of the contact line velocity ($\dot{x}$) to the withdrawal speed ($\dot{h}$) as a function of the contact line position (x_{cl}) for the 4 types of fibre from the model, calculated as the local slope of $h(x_{cl})$. According to the model the velocity goes to infinity in the static limit ($\dot{h} \to 0$) during the jump. However, an acceleration/deceleration event is difficult to distinguish from actual jumps since our experimental setup is not able to register the contact line position at $\dot{x}/\dot{h}$ ratios higher than 1.5 (a limitation of our experimental setup), as can be seen in Fig. 7b and c, where theoretical velocity values (blue lines) are compared with experimentally measured values (red circles) for a 150/100 and 150/140 fibre respectively. Accordingly, at very high wave amplitudes, the predicted and the experimentally measured jump positions are in agreement due to the fact that velocity raises to infinity sharply for fibres with high curvatures (see Fig. 7a). As the wave amplitude of the fibre is reduced, the contact line velocity increases more gently, and then the position at which our setup detects an apparent jump is far from the position at which theoretically infinite velocity is reached, or in the case of the 150/140 fibre a high acceleration event was inaccurately considered as a 'real jump'. When the maximum speed at which our camera can detect a jump ($\dot{x}/\dot{h} = 1.5$) is used for the calculation of the jump lengths, i.e. considering that the jump was produced at $\dot{x}/\dot{h} = 1.5$, then the model is fitting well also for high wave amplitude fibres (see corrected model data in Fig. 6a). As in the case of the experimental data, the model is also showing a clear relation between the geometry of the fibre and the displacement of the contact line after the jump. The model is also showing that the contact line slows down on the convex zone and speeds up on the concave zone of the fibre (see Fig. 7), in clear agreement with the experimental observations (see supporting material SM2).

A possible way to distinguish between an acceleration/deceleration event and a real jump would be to 'pause' the position of the bulk liquid h during a jump. If a jump length over the same portion of the fibre is observed, then a 'real' jump is observed, while if the jump is paused as well, it means that an acceleration/deceleration event was mistakenly taken as a jump. Another way is to perform experiments with different (still sufficiently low) immersion speeds. If the results for the different immersion speeds collapse in the representation of Fig. 7 upon the continuous line of the quasi-static prediction, then again, the observed acceleration/deceleration is not a real jump. The use of high speed cameras could also help to observe more accurately the position at which a jump is produced.

3.4. Full advancing-receding cycle

In this section, a full advancing-receding cycle is modelled by integrating a small-scale heterogeneity responsible for contact angle hysteresis. In contrast with previous sections where the angle with respect to the fibre θ_i was constant, we now impose a distribution of intrinsic contact angles $\theta_i(x_{CL})$. As in [37], a periodic distribution with a wavelength λ much smaller than the length scale of the experiment (i.e. the fibre dimensions) induces a nearly continuous range of metastable apparent angles θ_V at fixed h, while at the same time implying a constant θ_V when h is varied continuously, namely one of the limiting values, θ_A or θ_R, depending on whether h is increased or decreased. Thus, we incorporate the constant contact angle hysteresis measured on the perfectly cylindri-

cal parts of the fibre in the model under the form of a small-scale chemical heterogeneity (with $\lambda = 0.5\mu m$), calibrated in order to replicate the observed advancing angle θ_A and receding angle θ_R,

$$\cos(\theta_i(x_{CL})) = \frac{\cos(\theta_A) + \cos(\theta_R)}{2} + \frac{\cos(\theta_R) - \cos(\theta_A)}{2} \sin\left(\frac{2\pi x_{CL}}{\lambda}\right) \quad (7)$$

The prediction of this model for the 150/80 fibre compares very well with the measured tensiometer trace (black dots in Fig. 8). For the cylindrical portion of the fibre ($h < 100$), the static solutions (gray) appear as nearly continuous range at the scale of the graph, while being discontinuous at the sub-micron scale of λ. The green/red line is the subset of equilibrium solutions which is tracked upon increasing/decreasing h and corresponds to the limits of the solutions produced by small-scale jumps (invisible on graph), leading to a force which stays constant as a function of$h$. For the wavy portion of the fibre, the static solutions appear as multiple ranges at fixed h, the tracking of which now also requires jumps on the scale of the wavelength of the printed structure while the angle with respect to the fibre remains nearly constant.

4. Conclusions

Available experimental methodologies and models studying the meniscus shape and contact line movement during the wetting process of fibres deal almost exclusively with perfect circular cylinders [18–22]. While some work has been developed for shaped fibres [25,31,42], these have focused on fibres with complex cross section shapes but still constant along the fibre length.

In this paper, a novel experimental method combining tensiometry and goniometry was presented which enables a detailed description of the meniscus shape, contact line motion, and the corresponding contact angles on wavy fibres with different cross section shapes along the fibre length. The observation of liquid advancing and receding fronts on 4 different wavy fibres highlighted a stick-slip motion of the meniscus, the contact line jumping at well-defined positions depending on both the fibre surface curvature and its intrinsic wettability.

The stick-slip motion during the immersion and withdrawal of a wavy fibre in a liquid bath is described well by the proposed static model of capillary rise, assuming a distribution of radius along the fibre, and tracking the static solution upon increasing or decreasing the experimentally controlled immersion depth. This model expands on the methods used to model the stick-slip and contact angle hysteresis of a drop on chemically heterogeneous [33] and rough [43] substrates, and turns out to be considerably less involved mathematically than dynamic studies (see e.g. [44]). The model predictions are in good agreement with the experimental data. Furthermore, the relation between the geometry of the fibre and the jump length of the contact line can be clearly established, in agreement with our theoretical predictions. Deviations between experimental and model data for high wave amplitude fibres can be explained by acceleration/deceleration events that take place during the motion of the contact line on the curved surfaces. Also, it was shown that apparent contact angles on wavy fibres are a function of surface waviness, and can be corrected if fibre geometries are known. As assumed in the theory, the local real contact angle, which is obtained after correction for surface curvature, is constant.

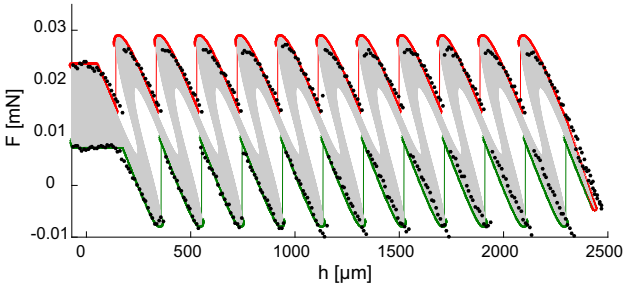

Fig. 8. Force predictions of the model (gray: all static solutions, green: advancing, red: receding) compared to tensiometer raw data (black dots), where chemical heterogeneity leading to contact angle hysteresis has been incorporated into the model. (For interpretation of the references to colour in this figure legend, the reader is referred to the web version of this article.)

In summary, the behaviour of the seemingly pinned and then jumping contact line, with associated big changes in apparent contact angles, θ_v, can be understood by the interplay of a constant local real contact angle of the material, θ_i, and the movement of the bulk liquid. This leads to storage of energy which is suddenly released when the contact line passes a given point of fibre curvature.

The analysis presented here is limited to sinusoidal wavy fibres but it can be extended to study the wetting behaviour of fibres with more complex shapes and at different dimensions scales, possibly helping to interpret the effect of roughness.

Acknowledgments

We gratefully acknowledge the financial support from ESA: European Space Agency and BELSPO: The Belgian Federal Science Policy Office through the PRODEX (Evaporation and Heat Transfer) and MAP (Evaporation and MANBO) project.

Appendix A. Supplementary material

Supplementary data to this article can be found online at https://doi.org/10.1016/j.jcis.2019.01.045.

References

[1] C.A. Fuentes, L.Q.N. Tran, M. Van Hellemont, V. Janssens, C. Dupont-Gillain, A. W. Van Vuure, I. Verpoest, Effect of physical adhesion on mechanical behaviour of bamboo fibre reinforced thermoplastic composites, Colloids Surf., A: Physicochem. Eng. Aspects 418 (2012) 7–15.
[2] D. Hansen, N. Bomholt, J.C. Jeppesen, A.C. Simonsen, Contact angle goniometry on single micron-scale fibers for composites, Appl. Surf. Sci. 392 (2017) 181–188.
[3] S. Qiu, C.A. Fuentes, D. Zhang, A.W. Van Vuure, D. Seveno, Wettability of a single carbon fiber, Langmuir 32 (38) (2016) 9697–9705.
[4] Y.-L. Hsieh, B. Yu, Liquid wetting, transport, and retention properties of fibrous assemblies: Part I: Water wetting properties of woven fabrics and their constituent single fibers, Text. Res. J. 62 (11) (1992) 677–685.
[5] L. Wilhelmy, Ueber die Abhängigkeit der Capillaritäts-Constanten des Alkohols von Substanz und Gestalt des benetzten festen Körpers, Annalen der Physik 195 (6) (1863) 177–217.
[6] A. Allan, Wilhelmy's plate and Young's equation, J. Colloid Sci. 13 (3) (1958) 273–274.
[7] L. Gao, T.J. McCarthy, Contact angle hysteresis explained, Langmuir 22 (14) (2006) 6234–6237.
[8] B. Prabhala, M. Panchagnula, V.R. Subramanian, S. Vedantam, Perturbation solution of the shape of a nonaxisymmetric sessile drop, Langmuir 26 (13) (2010) 10717–10724.
[9] T. Blake, Dynamic contact angles and wetting kinetics, Wettability 49 (1993) 251.
[10] T.D. Blake, The physics of moving wetting lines, J. Colloid Interface Sci. 299 (1) (2006) 1–13.
[11] Y. Yuan, T.R. Lee, Contact Angle and Wetting Properties, Surface Science Techniques, Springer, 2013, pp. 3–34.
[12] C.A. Fuentes, L.Q.N. Tran, C. Dupont-Gillain, W. Vanderlinden, S. De Feyter, A. W. Van Vuure, I. Verpoest, Wetting behaviour and surface properties of technical bamboo fibres, Colloids Surf., A: Physicochem. Eng. Aspects 380 (1–3) (2011) 89–99.
[13] Y.-N. Lee, S.-M. Chiao, Visualization of dynamic contact angles on cylinder and fiber, J. Colloid Interface Sci. 181 (2) (1996) 378–384.
[14] M.F. Pucci, P.-J. Liotier, S. Drapier, Capillary effects on flax fibers – modification and characterization of the wetting dynamics, Compos. A Appl. Sci. Manuf. 77 (2015) 257–265.
[15] D. Seveno, Dynamic Wetting of Fibers, Centre de recherche en modélisation moléculaire, Polytechnique de Mons, Belgium, 2004, p. 100.

[16] E. Atefi, J.A. Mann, H. Tavana, A robust polynomial fitting approach for contact angle measurements, Langmuir 29 (19) (2013) 5677–5688.
[17] A. Bateni, S.S. Susnar, A. Amirfazli, A.W. Neumann, A high-accuracy polynomial fitting approach to determine contact angles, Colloids Surf., A: Physicochem. Eng. Aspects 219 (1) (2003) 215–231.
[18] M. Vega, C. Gouttiere, D. Seveno, T. Blake, M. Voue, J. De Coninck, A. Clarke, Experimental investigation of the link between static and dynamic wetting by forced wetting of nylon filament, Langmuir 23 (21) (2007) 10628–10634.
[19] M.-J. Vega, D. Seveno, G. Lemaur, M.-H. Adão, J. De Coninck, Dynamics of the rise around a fiber: experimental evidence of the existence of several time scales, Langmuir 21 (21) (2005) 9584–9590.
[20] C. Clanet, D. Quéré, Onset of menisci, J. Fluid Mech. 460 (2002) 131–149.
[21] D.F. James, The meniscus on the outside of a small circular cylinder, J. Fluid Mech 63 (4) (1974) 657–664.
[22] K.M. Takahashi, Meniscus shapes on small diameter fibers, J. Colloid Interface Sci. 134 (1) (1990) 181–187.
[23] J. Wang, C.A. Fuentes, D. Zhang, X. Wang, A.W. Van Vuure, D. Seveno, Wettability of carbon fibres at micro-and mesoscales, Carbon 120 (2017) 438–446.
[24] L. Champougny, E. Rio, F. Restagno, B. Scheid, The break-up of free films pulled out of a pure liquid bath, J. Fluid Mech. 811 (2017) 499–524.
[25] M.M. Alimov, K.G. Kornev, Meniscus on a shaped fibre: singularities and hodograph formulation, Proc. R. Soc. A, R. Soc. (2014) 20140113.
[26] F.M. Orr, L.E. Scriven, A.P. Rivas, Menisci in arrays of cylinders: numerical simulation by finite elements, J. Colloid Interface Sci. 52 (3) (1975) 602–610.
[27] J.F. Joanny, P.G.D. Gennes, A model for contact angle hysteresis, J. Chem. Phys. 81 (1) (1984) 552–562.
[28] M. Hucker, I. Bond, A. Foreman, J. Hudd, Optimisation of hollow glass fibres and their composites, Adv. Compos. Lett. 8 (4) (1999) 181–189.
[29] I. Aranberri-Askargorta, T. Lampke, A. Bismarck, Wetting behavior of flax fibers as reinforcement for polypropylene, J. Colloid Interface Sci. 263 (2) (2003) 580–589.
[30] H.D. Wagner, Intermittent interfaces: bioinspired strategies towards material, 21st International Conference on Composite Materials, Xi'ann China, 2017.
[31] M.M. Alimov, K.G. Kornev, Singularities of meniscus at the V-shaped edge, Mech. Res. Commun. 62 (2014) 162–167.
[32] M. Nosonovsky, Multiscale roughness and stability of superhydrophobic biomimetic interfaces, Langmuir 23 (6) (2007) 3157–3161.
[33] A. Marmur, Contact angle hysteresis on heterogeneous smooth surfaces, J. Colloid Interface Sci. 168 (1) (1994) 40–46.
[34] M.E. Shanahan, Simple theory of‘‘ stick-slip” wetting hysteresis, Langmuir 11 (3) (1995) 1041–1043.
[35] H. Tavana, G. Yang, C.M. Yip, D. Appelhans, S. Zschoche, K. Grundke, M.L. Hair, A.W. Neumann, Stick– slip of the three-phase line in measurements of dynamic contact angles, Langmuir 22 (2) (2006) 628–636.
[36] M. Shanahan, K. Sefiane, Kinetics of triple line motion during evaporation, Contact Angle, Wettability .ion 6 (2009) 19–31.
[37] M. Hatipogullari, C. Wylock, M. Pradas, S. Kalliadasis, P. Colinet, Contact angle hysteresis in a microchannel: statics, Phys. Rev. Fluids (2018). https://journals.aps.org/prfluids/accepted/00076S4bDd51db0550005a09fc75a013220021635.
[38] E. Decker, S. Garoff, Using vibrational noise to probe energy barriers producing contact angle hysteresis, Langmuir 12 (8) (1996) 2100–2110.
[39] C.A. Fuentes, K. Beckers, H. Pfeiffer, L. Tran, C. Dupont-Gillain, I. Verpoest, A. Van Vuure, Equilibrium contact angle measurements of natural fibers by an acoustic vibration technique, Colloids Surf., A: Physicochem. Eng. Aspects 455 (2014) 164–173.
[40] R.E. Johnson Jr, R.H. Dettre, D.A. Brandreth, Dynamic contact angles and contact angle hysteresis, J. Colloid Interface Sci. 62 (2) (1977) 205–212.
[41] M. Delmas, M. Monthioux, T. Ondarçuhu, Contact angle hysteresis at the nanometer scale, Phys. Rev. Lett. 106 (13) (2011) 136102.
[42] S. Zhu, D.E. Hirt, Improving the wettability of deep-groove polypropylene fibers by photografting, Text. Res. J. 79 (6) (2009) 534–547.
[43] C. Huh, S. Mason, Effects of surface roughness on wetting (theoretical), J. Colloid Interface Sci. 60 (1) (1977) 11–38.
[44] C. Wylock, M. Pradas, B. Haut, P. Colinet, S. Kalliadasis, Disorder-induced hysteresis and nonlocality of contact line motion in chemically heterogeneous microchannels, Phys. Fluids 24 (3) (2012) 032108.